



The directional isotropy of LIGO-Virgo binaries

MAXIMILIANO ISI ,¹ WILL M. FARR ,^{1,2} AND VIJAY VARMA ^{3,4,*}

⁵*Center for Computational Astrophysics, Flatiron Institute, 162 5th Ave, New York, NY 10010*

⁶*Department of Physics and Astronomy, Stony Brook University, Stony Brook NY 11794, USA*

⁷*Max Planck Institute for Gravitational Physics (Albert Einstein Institute), Am Mühlenberg 1, Potsdam 14476, Germany*

⁸*Department of Mathematics, Center for Scientific Computing and Data Science Research, University of Massachusetts, Dartmouth, MA 02747, USA*

(Dated: May 3, 2023)

ABSTRACT

We demonstrate how to constrain the degree of absolute alignment of the total angular momenta of LIGO-Virgo binary black holes, looking for a special direction in space that would break isotropy. We also allow for inhomogeneities in the distribution of black holes over the sky. Making use of dipolar models for the spatial distribution and orientation of the sources, we analyze 57 signals with false-alarm rates $\leq 1/\text{yr}$ from the third LIGO-Virgo observing run. Accounting for selection biases, we find the population of LIGO-Virgo black holes to be fully consistent with both homogeneity and isotropy. We additionally find the data to constrain some directions of alignment more than others, and produce posteriors for the directions of total angular momentum of all binaries in our set. All code and data are made publicly available in <https://github.com/maxisi/gewisotropy/>.

1. INTRODUCTION

With the increasing number of BBHs detected by LIGO (Aasi et al. 2015) and Virgo (Acernese et al. 2015), it has become possible to study the distribution of such gravitational wave (GW) sources over time and space (Abbott et al. 2021a; Fishbach et al. 2018, 2021; Stiskalek et al. 2021; Payne et al. 2020; Cavaglia & Modi 2020; Essick et al. 2023). Since BBHs can be detected up to nonnegligible redshifts (currently, $\lesssim 1$), we expect their distribution at large scales to reflect the homogeneity and isotropy that characterize the universe cosmologically—a departure from that expectation would reveal a major shortcoming in our understanding of the detection biases affecting the LIGO-Virgo instruments, or, more tantalizingly, point to fundamentally new physics or astrophysics.

misi@flatironinstitute.org

will.farr@stonybrook.edu

vijay.varma@aei.mpg.de

* Marie Curie fellow

The homogeneity (Stiskalek et al. 2021; Payne et al. 2020; Cavaglia & Modi 2020; Essick et al. 2023) and isotropy (Vitale et al. 2022) of BBHs have been studied before under different frameworks. In this work, we reconsider the problem from a new point of view by quantifying the degree of alignment of the BBH orbits; in other words, we ask the question: could the total angular momentum vectors of LIGO-Virgo BBHs be preferentially aligned with a special direction in space? We consider this possibility as we simultaneously search for angular inhomogeneities in the spatial distribution of sources, thus constraining the existence of special directions controlling both the alignment and location of BBHs.

Unlike previous studies, we look for a breaking of isotropy in the angular momenta through the existence of a special direction in space with reference to some absolute frame, like the cosmic microwave background or far away stars (Fig. 1, second panel), and not with respect to Earth. The discovery of such a special direction could reveal the presence of a vector field breaking Lorentz symmetry. This differs from previous works like Vitale et al. (2022), which checked for anomalies in the alignment of sources with respect to Earth, as reflected

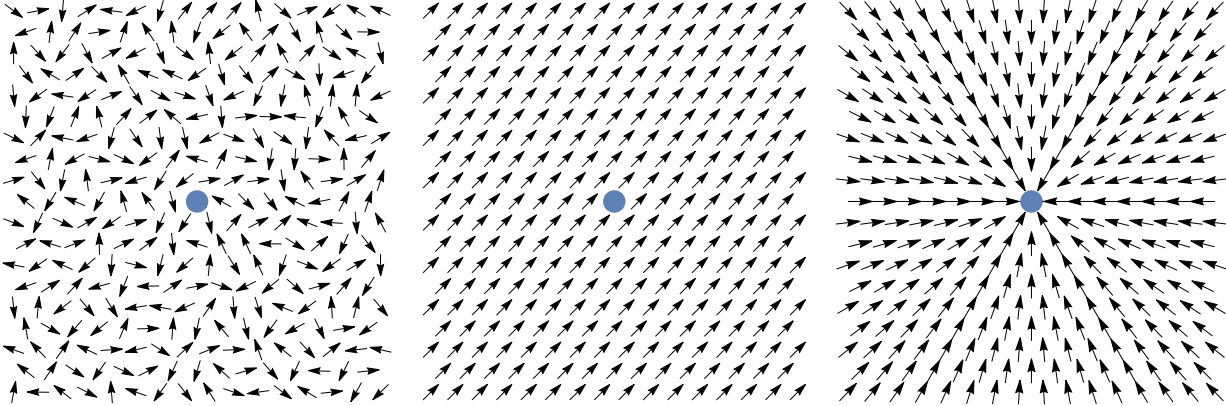


Figure 1. *BBH orientation models.* By default, we expect BBH angular momenta (arrows) to be oriented randomly with respect to Earth (circle) or each other, reflecting isotropy (first panel). In this study, we consider the possibility that BBH orbits follow a special direction in space, the extreme of which is full alignment (second panel). Previous studies, like Vitale et al. (2022), have considered models in which binaries are (or are perceived to be) aligned anomalously with respect to Earth, e.g., pointing preferentially towards it (third panel). The first two panels both have a distribution of inclinations that looks isotropic to analyses like Vitale et al. (2022).

in the distribution of BBH inclinations relative to the line of sight (Fig. 1, third panel). Such studies are not sensitive to the kind of overall alignment in absolute space that we look for here.

In Sec. 2 we describe the population model we use to constrain anisotropies, as well as our assumptions about the astrophysical distribution of BBH properties like masses and redshifts, and our treatment of selection biases. In Sec. 3 we outline the data products used in our analysis. We present our results in Sec. 4, including constraints on the degree of orientation and location inisotropies, as well as maps of possible preferred directions. In Sec. 5, we summarize validation tests of our infrastructure to contextualize our measurement. We conclude in Sec. 6. Appendices show how to obtain posteriors on the angular-momentum direction, discuss hypperparameter prior choices and display posteriors for the angular-momentum direction for all events in our set.

2. METHOD

2.1. Isotropy modeling

In order to study the spatial distribution and orientation of BBHs, we must analyze the collection of detections under a hierarchical population model that allows for variable degrees of spatial and directional correlations (see, e.g., Essick et al. 2023). This requires modeling the distribution of source locations, \hat{N} , and total-angular-momentum directions, \hat{J} . For modeling purposes, the \hat{N} and \hat{J} vectors must be expressed through their Cartesian components in some absolute reference frame.

We choose to work in geocentric, equatorial celestial coordinates, with the vernal equinox as the x axis. In

that frame, the sky-location vector is, for each BBH,

$$\hat{N} = (\cos \alpha \cos \delta, \sin \alpha \cos \delta, \sin \delta), \quad (1)$$

for the right ascension α and declination δ ; meanwhile, the orientation vector is $\hat{J} \equiv \vec{J}/|\vec{J}|$ where

$$\vec{J} = \vec{L} + \vec{S}_1 + \vec{S}_2, \quad (2)$$

for the orbital angular momentum \vec{L} and individual (dimensionful) black hole (BH) spin angular momenta $\vec{S}_{1/2}$. The Cartesian components of \hat{J} can be computed in the above frame as a function of α , δ , and the polarization angle ψ (Isi 2022), as well as the component masses $m_{1/2}$, the dimensionless spin vectors $\vec{\chi}_{1/2}$ and the orbital phase ϕ_{ref} at some reference frequency f_{ref} ; we outline this calculation in Appendix A and release relevant code in Isi et al. (2023). We prefer to work with \hat{J} rather than \vec{L} because the former is conserved over the coalescence to a high degree, even for precessing systems (Poisson & Will 2014).

Our goal is to quantify the degree of isotropy in \hat{N} and \hat{J} . To this end, we model each of those vectors as drawn from an isotropic distribution with a dipolar correction of variable magnitude. This *ad hoc* modification may be generally seen as the first term in a harmonic expansion around isotropy, and is specifically well suited to capture the existence of a preferred direction in space. The dipolar components in the location and orientation distributions are defined by dipole vectors $\vec{v}_{N/J}$ whose magnitudes control the degree of deviation from isotropy for \hat{N} and \hat{J} respectively.

Concretely, we implement the following population-level likelihood for each event (indexed by i)

$$p(\hat{N}_i, \hat{J}_i | \vec{v}_N, \vec{v}_J) \sim \frac{1}{16\pi^2} (1 + \vec{v}_N \cdot \hat{N}_i) (1 + \vec{v}_J \cdot \hat{J}_i), \quad (3)$$

for some special-direction vectors $\vec{v}_{N/J}$, with $0 \leq |\vec{v}_{N/J}| < 1$, to be inferred as hyperparameters from the collection of detections. The fully isotropic case is covered for $\vec{v}_N = \vec{v}_J = 0$. On the other hand, setting $\vec{v}_J = 0$ alone allows for a nonhomogenous distribution of sources in the sky while assuming isotropic source orientations; this reduces to the “dipole” model in [Essick et al. \(2023\)](#). Modeling the likelihood as in Eq. (3), with $|\vec{v}_{N/J}| < 1$, ensures that the likelihood itself remains positive everywhere.

It is convenient to rephrase the constraint that $0 \leq |\vec{v}_{N/J}| < 1$ by re-parameterizing the population in Eq. (3), through two corresponding, auxiliary vectors $\vec{u}_{N/J}$ defined such that

$$\vec{v}_{N/J} = \frac{\vec{u}_{N/J}}{\sqrt{1 + |\vec{u}_{N/J}|^2}}. \quad (4)$$

In this way, we ensure $0 \leq |\vec{v}_{N/J}| \leq 1$ for $-\infty < \vec{u}_{N/J} < \infty$; $\vec{u}_{N/J}$ are unconstrained. This “decompactifying” transformation is more effective for sampling purposes than enforcing a sharp constraint on the magnitudes of $\vec{v}_{N/J}$. For small $|\vec{v}_{N/J}| \ll 1$, $\vec{v}_{N/J} \simeq \vec{u}_{N/J}$ to second order in $|\vec{v}_{N/J}|$. As a prior, we choose a three-dimensional Gaussian distribution on the components of each \vec{u}_N and \vec{u}_J , with zero mean and standard deviation $\sigma = 0.4$. This choice of prior is designed to be fairly uninformative about $\vec{v}_{N/J}$ (i.e., lacking a strong gradient) while still peaking at $\vec{v}_{N/J} = \vec{0}$; see Appendix B for a description of this feature.

2.2. Reweighting to an astrophysical population

Besides the location and orientation modeling described above, we need to ensure that our assumptions about the parameters of each individual BBH, like masses and redshift, are astrophysically sensible. To that end, we assume a redshift distribution that follows the Madau-Dickinson star formation rate ([Madau & Dickinson 2014](#)) in the comoving frame. For the masses, we assume a prior distribution inversely proportional to the heaviest component mass ($\propto 1/m_1$) and uniform in the mass ratio (constant in $q = m_2/m_1$), and restrict our sample to BHs with (posterior-median) masses in the range $5 M_\odot < m_2 \leq m_1 < 150 M_\odot$; within that range, this choice is a simple approximation to the measurement in [Abbott et al. \(2021a\)](#). We assume the population of component spins are isotropically oriented with

Table 1. Events considered.

GW190408_181802	GW190708_232457	GW191129_134029
GW190412_053044	GW190719_215514	GW191204_171526
GW190413_052954	GW190720_000836	GW191215_223052
GW190413_134308	GW190727_060333	GW191216_213338
GW190421_213856	GW190728_064510	GW191222_033537
GW190503_185404	GW190731_140936	GW191230_180458
GW190512_180714	GW190803_022701	GW200112_155838
GW190513_205428	GW190805_211137	GW200128_022011
GW190517_055101	GW190828_063405	GW200129_065458
GW190519_153544	GW190828_065509	GW200202_154313
GW190521_030229	GW190910_112807	GW200208_130117
GW190521_074359	GW190915_235702	GW200209_085452
GW190527_092055	GW190925_232845	GW200216_220804
GW190602_175927	GW190929_012149	GW200219_094415
GW190620_030421	GW190930_133541	GW200224_222234
GW190630_185205	GW191103_012549	GW200225_060421
GW190701_203306	GW191105_143521	GW200302_015811
GW190706_222641	GW191109_010717	GW200311_115853
GW190707_093326	GW191127_050227	GW200316_215756

respect to the orbital angular momentum, with a uniform distribution over their dimensionless magnitude;¹ we control for this assumption in Sec. 5.2. A future analysis may fit the astrophysical distribution of these parameters jointly with the orientation and location of the binaries.

2.3. Selection biases

Since we are attempting to model the *intrinsic* distribution of all BBH sources, not merely those that were detected, we must account for the difference in LIGO-Virgo’s sensitivity to various sources. This is true for both intrinsic parameters, like BH masses and spin magnitudes, as well as the location and orientation parameters in which we are interested for this work (namely, \hat{N} and \hat{J}). With knowledge of the instruments’ sensitivity over parameter space, we use the measured selection function to obtain a measurement of the intrinsic distribution of parameters out of the distribution of detected sources ([Loredo 2004; Mandel et al. 2019](#)).

Evaluating the detectors’ sensitivity over parameter space requires large simulation campaigns that quantify the end-to-end performance of LIGO-Virgo detection pipelines by injecting and recovering synthetic signals. As in [Essick et al. \(2023\)](#), we take advantage of the BBH dataset in [Abbott et al. \(2021b\)](#) for this purpose.² Since this injection campaign only covered LIGO-Virgo’s third observing run, we only consider events detected during

¹ This implies that our modeling of \hat{J} following Eq. (3) can be reinterpreted as a nontrivial modeling of \vec{L} through Eq. (2).

² Specifically, the `endo3_bbhpop-LIGO-T2100113-v12` injection set.

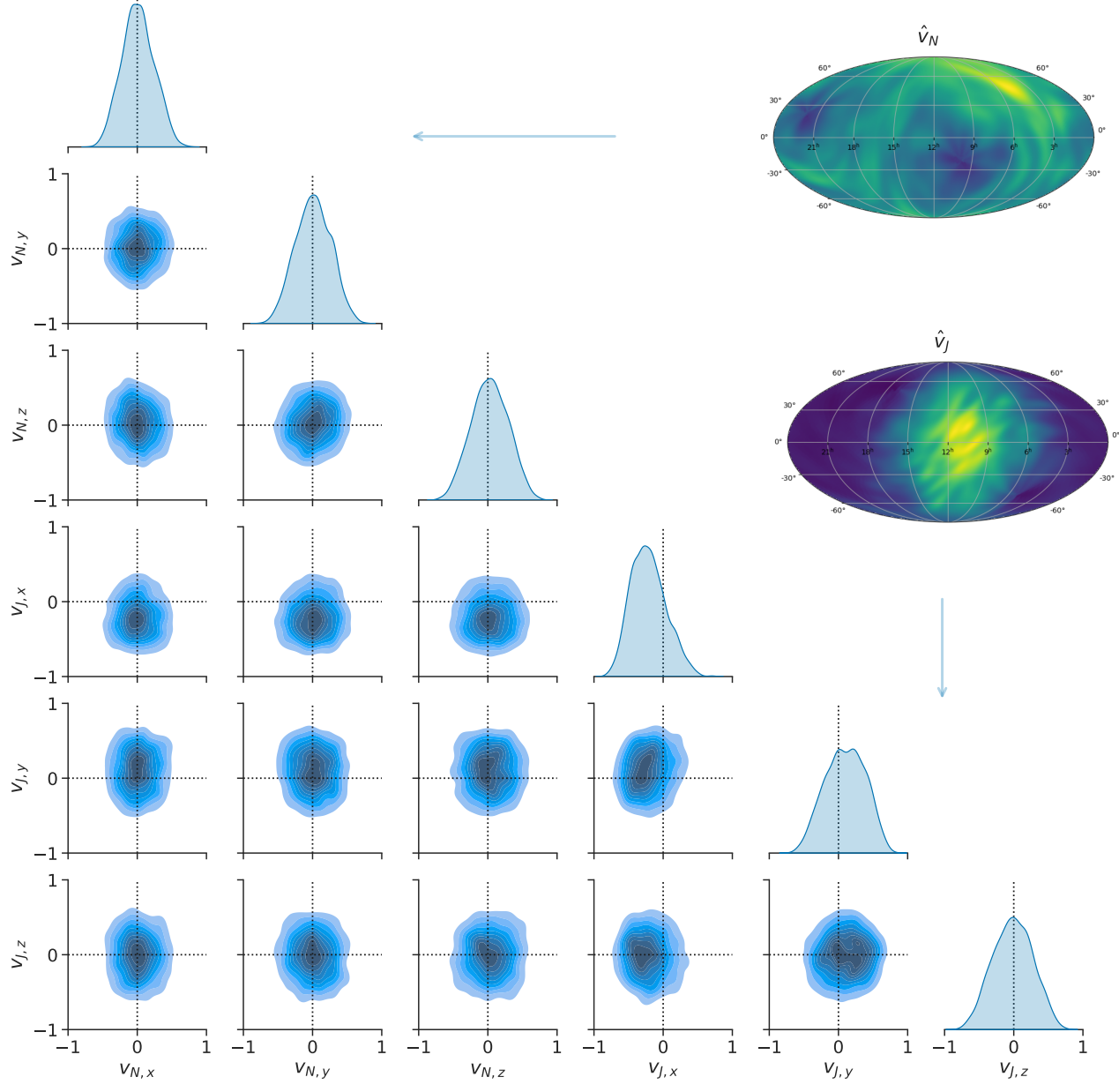


Figure 2. *Isotropy measurement.* Result of the simultaneous measurement of location and orientation isotropy through the model in Eq. (3), as represented by the posterior distribution on the dipole vectors $\vec{v}_{N/J}$ (corner plot), and the corresponding projections over the sky (Mollweide insets). The six-dimensional posterior distribution is represented through credible levels over two-dimensional slices (blue contours, spaced at intervals corresponding to 10% increments in probability mass, with the outer contour enclosing 90% of the probability), and one-dimensional marginals (diagonal). The upper-left and lower-right sub-corners encode constraints on the individual components of each \vec{v}_N and \vec{v}_J respectively (highlighted with vertical and horizontal lines in the margin), while the other panels encode potential correlations between the location and orientation inisotropies. The measurements for $\vec{v}_{N/J}$ can be projected into distribution over the sky as in the top-right insets, which show the allowed dipole orientations for $\hat{v}_N \equiv \vec{v}_N / |\vec{v}_N|$ (top) or $\hat{v}_J \equiv \vec{v}_J / |\vec{v}_J|$ (bottom), with lighter colors encoding higher probability density over the celestial sphere (Singer 2018; Singer et al. 2016a,b); inhomogeneities in these sky-maps do not constitute evidence for anisotropies. Isotropy is recovered for $\vec{v}_N = \vec{v}_J = 0$ (dotted lines), which is well supported by the 6D posterior.



that period; together with the mass constraints cited above, this means there are 57 BBH events to be included in our analysis (listed in Table 1).

97

3. DATA

Our analysis starts from posterior samples for individual events reported by LIGO-Virgo in Abbott et al. (2021c,d) and publicly released in Abbott et al. (2022, 2021e) through the Gravitational Wave Open Science Center (Abbott et al. 2021f,g,h). Specifically, we make use of results obtained with the IMRPhenomXPHM waveform (Pratten et al. 2021, 2020; García-Quirós et al. 2020, 2021) that have been already reweighted to a distance prior uniform in comoving volume. The single-event inference was carried out by the LIGO-Virgo collaborations using the BILBY parameter estimation pipeline (Romero-Shaw et al. 2020; Ashton et al. 2019), as detailed in Abbott et al. (2021c,d). We reweight those samples following the astrophysical population described above (see, e.g., Miller et al. 2020; Essick & Farr 2022, for methodology) and then use them to produce distributions for the components of \hat{N} and \hat{J} , which we use as input for our hierarchical analysis based on Eq. (3).

The six-dimensional posteriors for the components of \hat{J} and \hat{N} for each event are the primary input for our hierarchical isotropy analysis. We show the posteriors for \hat{J} in Fig. 8 as skymaps for all events in our set, produced using standard LIGO-Virgo tools for representing probability densities over the sky (Singer 2018; Singer et al. 2016a,b); we make these posteriors, resulting from the calculation detailed in Appendix A, available in our data release (Isi et al. 2023). The equivalent figures for \hat{N} are nothing but the sky-localization maps already made available by LIGO-Virgo (Abbott et al. 2022, 2021e).

4. RESULTS

We showcase the full result of our analysis in Fig. 2, which represents the simultaneous measurement of location and orientation anisotropies through the six-dimensional posterior on the components of \vec{v}_N and \vec{v}_J . The result is fully consistent with both kinds of isotropy, with $\vec{v}_N = 0$ and $\vec{v}_J = 0$ supported with high credibility, falling close to the peak of the marginal distributions on the 1% and 43% quantiles respectively;³ this feature is also reflected in the fact that the origin is well supported in all the panels of the corner plot in Fig. 2. The result for \vec{v}_N is consistent with previous studies (Essick et al.

³ These three-dimensional quantiles correspond to the fraction of $\vec{v}_{J/N}$ samples with higher probability density than the origin.

2023), which did not find evidence against isotropy in the location of LIGO-Virgo sources.

To the extent that there is any support for nonzero dipolar contributions to the location or orientation densities (namely, for $|\vec{v}_{J/N}| > 0$), their possible directions in the sky are represented by the insets on the top right of Fig. 2: a higher density indicates a potentially allowed orientation for the \vec{v}_N (top) or \vec{v}_J (bottom) dipole vectors. These skymaps reveal that the data are not in conflict with the existence of a weak dipole along the vernal equinox in the celestial equatorial plane (the direction of the x axis in our Cartesian coordinate system), as implied by the marginal on $\vec{v}_{J,x}$ in Fig. 2; this dipole is allowed, but not required, by the data, since the posterior is fully consistent with $\vec{v}_J = 0$.

Indeed, although inhomogeneities appear in these Mollweide projections, this should not be interpreted as evidence for anisotropies: the density of points in those maps only encodes *permissible* directions for the dipole, without implications for its magnitude. In fact, inhomogeneities will appear in such plots any time the posterior does not happen to peak exactly at the three-dimensional origin of $\vec{v}_{J/N}$, as we expect to be commonly the case even if $\vec{v}_{J/N} = \vec{0}$ is the underlying truth.⁴

In Fig. 3, we provide an additional representation of this posterior projected onto the three-dimensional spaces of \vec{v}_J and \vec{v}_N ; we also present the prior for comparison. Large dipolar contributions are disfavored by the posterior in all cases, and the posterior distributions are more concentrated than the prior, indicating that the data are informative. The posterior standard deviations for the three Cartesian components of \vec{v}_J and \vec{v}_N are smaller by $\{19\%, 9\%, 9\%\}$ and $\{25\%, 19\%, 15\%\}$ respectively with respect to the prior. The stronger tightening in the \vec{v}_N distribution is a consequence of \hat{N} being better constrained than \hat{J} in individual events. Figure 3 again makes it apparent that data disfavor certain directions for the \vec{v}_J dipole (towards the positive- x quadrants, away from the vernal equinox).

We may translate the result in Fig. 2 into a posterior on the magnitudes $|\vec{v}_{J/N}|$ of the dipole components, as we do in Fig. 4. However, the one-dimensional posteriors on these quantities is heavily dominated by the dimensionality of the problem, which results in a Jacobian disfavoring small values of $|\vec{v}_{J/N}|$ due to the limited phase

⁴ With a finite number of events in the catalog, even if $\vec{v}_{J/N}$ is zero in truth, the maximum-likelihood estimate will not, in general, be zero. The posterior will therefore peak away from zero (but be fully consistent with zero). In this situation inhomogeneity can appear as in Fig. 2.

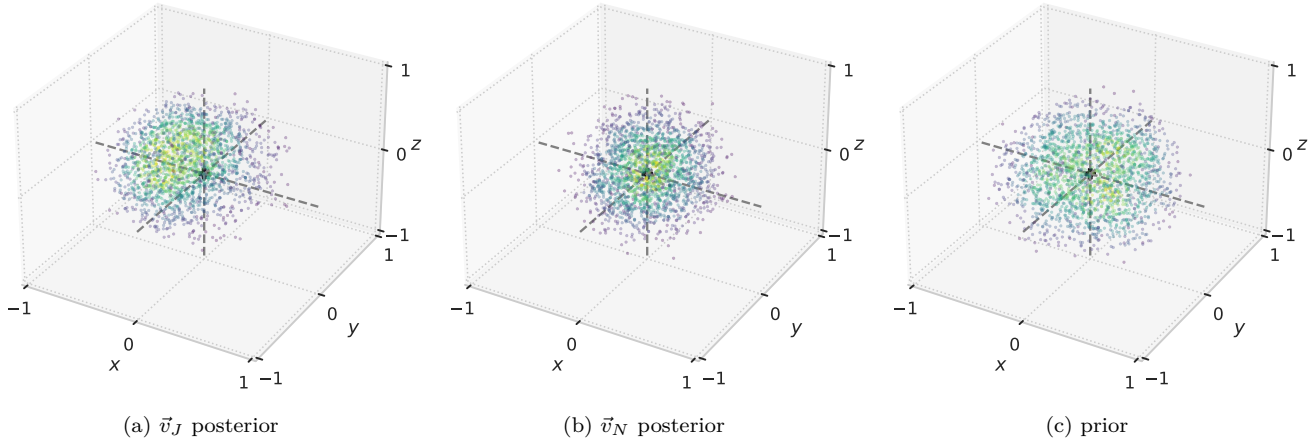


Figure 3. 3D distributions. Three-dimensional representation of the $\vec{v}_{J/N}$ measurement in Fig. 2 (first two panels), in comparison to the prior (last panel). Each point is drawn from the corresponding three-dimensional distribution, with color proportional to the probability density (lighter colors for higher density). The origin, representing isotropy, is well favored in all cases (intersection of gray dashed lines). The posteriors are tighter with respect to the prior, as is also seen in Fig. 4.

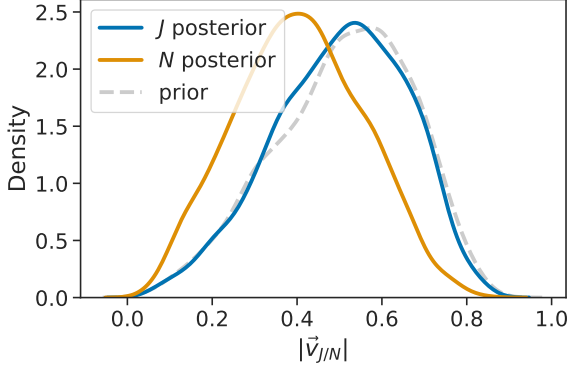


Figure 4. Posterior on dipole magnitudes. The measurement of Fig. 2 translated into one-dimensional posteriors on the $|\vec{v}_J|$ (blue) and $|\vec{v}_N|$ (orange) magnitudes. These are shifted rightward with respect to the implied prior (gray), which itself heavily disfavors $|\vec{v}_{J/N}| = 0$ due to the reduced phase space near the origin in a three-dimensional space.

space near $\vec{v}_J = 0$ or $\vec{v}_N = 0$.⁵ Therefore, even though our three-dimensional prior does not treat $\vec{v}_{J/N} = 0$ as a special point (Appendix B), the effective prior induced on the magnitudes heavily disfavors the origin in $|\vec{v}_{J/N}|$ due to the reduced available prior volume (gray curve in Fig. 4); that explains why the posteriors in Fig. 4 themselves appear to disfavor $|\vec{v}_{J/N}| = 0$. With that in mind, the influence of the data can be seen in the leftward shift

⁵ In other words, although the probability density is high near the origin, this is outweighed by the greater volume found far away, so that the overall probability of finding $\vec{v}_{J/N} = 0$ is small. Any density in $\vec{v}_{J/N}$ that is finite at the origin will produce a density on $|\vec{v}_{J/N}|$ that behaves as $|\vec{v}_{J/N}|^2$ near the origin.

of the $|\vec{v}_{J/N}|$ distributions with respect to the prior; this effect is more pronounced for \vec{v}_N , which is a consequence of the fact that \vec{N} is generally better measured than \vec{J} . Although the shift in $|\vec{v}_J|$ is slight, the data are informative about \vec{v}_J —constraining some of its possible orientations (Figs. 2 and 3), if not its overall magnitude.

5. VALIDATION

In this section, we validate our setup by studying simulated datasets in which \hat{J} and \hat{N} are isotropically distributed (5.1). We also revisit our assumptions about the astrophysical distribution of BBH parameters, described in Sec. 2.2, and show that they are robust.

5.1. Injections from selection set

We validate our infrastructure on the set of injections used to evaluate the selection function of the instruments, which was drawn from an intrinsically isotropic distribution (Abbott et al. 2021b). This provides an end-to-end test of our setup, including the computation of location and orientation vectors, the selection function and the inference process.

Concretely, we simulate catalogs of detections drawn from the injection set used to evaluate the selection function as described in Sec. 2.3 (Abbott et al. 2021b). For simplicity, we treat the injection parameters as a single sample of a fictitious posterior: the input to our hierarchical analysis is one sample per synthetic event, drawn from the distribution in Sec. 2.3. At each iteration, we double the size of the simulated catalog. Since the injection distribution was constructed to be isotropic (Abbott et al. 2021b), we expect this experiment to indicate $\vec{v}_{J/N} = \vec{0}$, with certainty growing with catalog size.

We show the result in Fig. 5 for \vec{v}_J (the result for \vec{v}_N is similar). As expected, $\vec{v}_{J/N} = \vec{0}$ is supported with increasing certainty as the synthetic catalog grows. This is what we expect if our infrastructure is working as designed.

329 5.2. Astrophysical distributions

330 As described, in Sec. 2.2, analysis above (Figs. 2–4)
 331 hinged on simplified assumptions about the astrophys-
 332 ical distribution of BH masses, spins and redshifts. To
 333 evaluate the impact of this simplification, we repeat our
 334 analysis but now reweighting to a different astrophys-
 335 ical population based on the measurements in Abbott
 336 et al. (2021a). Specifically, we make use of the highest-
 337 probability instantiation of the POWER LAW + PEAK
 338 parametric mass model and the DEFAULT spin model,
 339 with parameters obtained from the posterior samples
 340 released in Abbott et al. (2023). This model treats the
 341 astrophysical distribution of BH masses as a power law
 342 plus a Gaussian peak, with density evolving over co-
 343 moving volume as a power law; the spins are isotropic
 344 with a possible Gaussian overdensity in alignment with
 345 the orbital angular momentum, and with magnitudes
 346 following a Beta distribution (see (Abbott et al. 2021a)
 347 for details). To implement this new astrophysical prior,
 348 both individual detections and the selection injections
 349 are reweighted accordingly.

350 The result of assuming this different astrophysical dis-
 351 tribution is shown in Fig. 6, compared to the main result
 352 above. Although the new posterior differs slightly from
 353 our primary one in Fig. 2, as we might expect given
 354 the difference in models, the change is quite limited and
 355 does not qualitatively impact the discussion above. The
 356 discrepancy is somewhat more pronounced for the com-
 357 ponents of \vec{v}_J , as we might expect from the fact that
 358 the reconstruction of \hat{J} must factor our inference on the
 359 masses and three dimensional spins of each BBH. In the
 360 future, a more comprehensive analysis might simultane-
 361 ously measure $\vec{v}_{J/N}$ and the distribution of astrophysical
 362 properties.

363 6. CONCLUSION

364 We have demonstrated a measurement constraining
 365 the potential alignment of the total angular momenta of
 366 BBHs detected by LIGO and Virgo, using 57 detections
 367 from their third observing run and duly accounting for
 368 selection effects. In addition to alignment of momenta,
 369 we simultaneously looked for inhomogeneities in the dis-
 370 tribution of sources over the sky. We found no evidence
 371 against isotropy in either the orientation or, consistent
 372 with previous works, the location of LIGO-Virgo BBHs.
 373 Additionally, we determined that the GWTC-3 data

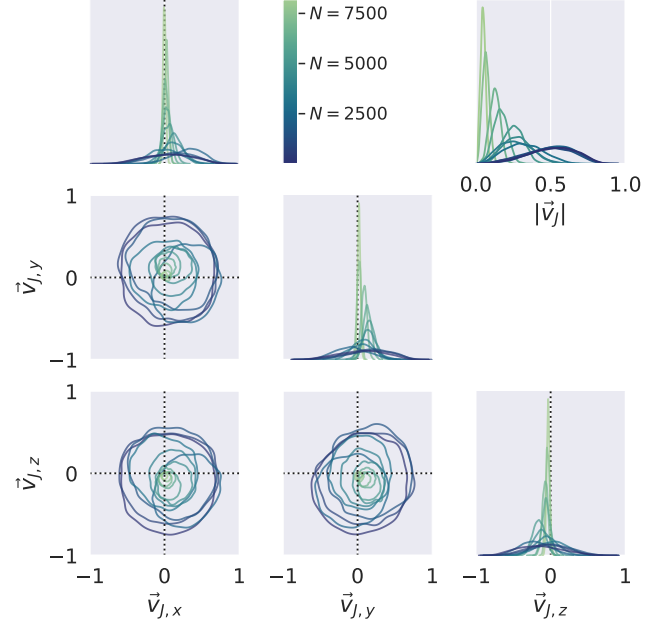


Figure 5. Validation on synthetic catalogs drawn from selection injection set. Result of hierarchical analyses on synthetic catalogs of increasing size N (color), obtained by taking draws from the injection set used to evaluate the selection function (Sec. 2.3) and using them as single samples from the \hat{J} and \hat{N} posterior of synthetic events. We show the posterior on the components of \vec{v}_J (main corner), and the implied posterior on the magnitude $|\vec{v}_J|$ (upper right). A lighter color corresponds to a larger catalog: starting with $N = 4$ events for the darkest color and progressively doubling the catalog size 11 times to reach $N = 8192$ events for the lightest color. The hierarchical analysis measures $\vec{v}_J = \vec{0}$ with growing precision as the size of the catalog increases.

374 disfavor certain orientations of the potential preferred
 375 alignment of angular momenta more than others.

376 Future measurements will improve as the LIGO, Virgo
 377 and KAGRA detectors grow in sensitivity, resulting in
 378 many more detections at higher signal-to-noise ratios,
 379 which will result in more precise isotropy constraints.
 380 The advent of next generation detectors, like Cosmic
 381 Explorer (Dwyer et al. 2015; Abbott et al. 2017; Re-
 382 itze et al. 2019) or the Einstein Telescope (Punturo
 383 et al. 2010), will enable the exploration of higher order
 384 anisotropies and other interesting effects, like correla-
 385 tions with redshift or, potentially, local correlations in
 386 the directions \hat{N} and \hat{J} on the sky.

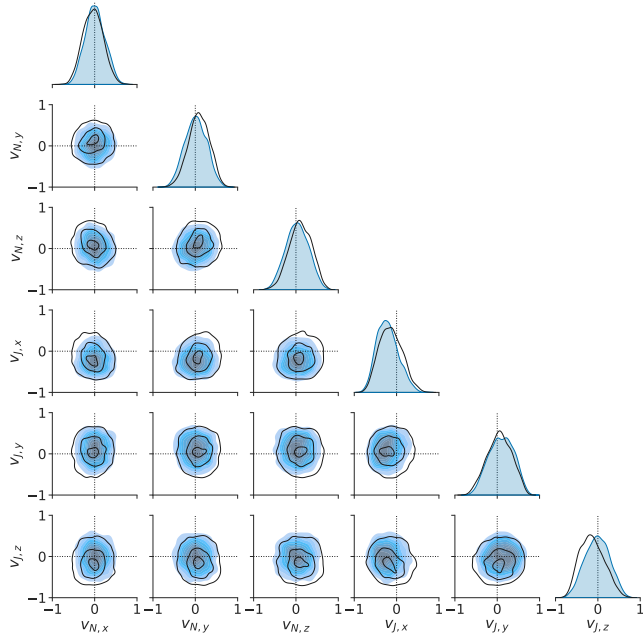


Figure 6. *Effect of astrophysical population.* We repeat the isotropy analysis with a different assumption about the underlying distribution of BBH parameters based on the measurement in Abbott et al. (2021a). This yields the result shown in black, as opposed to the result in Fig. 2, which is reproduced here in blue for comparison. The black contours enclose 90%, 50% and 10% of the marginal probability mass.

We thank Reed Essick for valuable comments. The Flatiron Institute is a division of the Simons Foundation. V.V. acknowledges funding from the European Union’s Horizon 2020 research and innovation program under the Marie Skłodowska-Curie grant agreement No. 896869. This material is based upon work supported by NSF’s LIGO Laboratory which is a major facility fully funded by the National Science Foundation. This research has made use of data or software obtained from the Gravitational Wave Open Science Center (gw-openscience.org), a service of LIGO Laboratory, the LIGO Scientific Collaboration, the Virgo Collaboration, and KAGRA. LIGO Laboratory and Advanced LIGO are funded by the United States National Science Foundation (NSF) as well as the Science and Technology Facilities Council (STFC) of the United Kingdom, the Max-Planck-Society (MPS), and the State of Niedersachsen/Germany for support of the construction of Advanced LIGO and construction and operation of the GEO600 detector. Additional support for Advanced LIGO was provided by the Australian Research Council. Virgo is funded, through the European Gravitational Observatory (EGO), by the French Centre National de Recherche Scientifique (CNRS), the Italian Istituto Nazionale di Fisica Nucleare (INFN) and the Dutch Nikhef, with contributions by institutions from Belgium, Germany, Greece, Hungary, Ireland, Japan, Monaco, Poland, Portugal, Spain. The construction and operation of KAGRA are funded by Ministry of Education, Culture, Sports, Science and Technology (MEXT), and Japan Society for the Promotion of Science (JSPS), National Research Foundation (NRF) and Ministry of Science and ICT (MSIT) in Korea, Academia Sinica (AS) and the Ministry of Science and Technology (MoST) in Taiwan. This is a reproducible article compiled with SHOWYOURWORK (Luger et al. 2021). This paper carries LIGO document number LIGO-P2300088.

Software: PYMC (Wiecki et al. 2023), ARVIZ (Martín et al. 2023), NUMPY (Harris et al. 2020), SCIPY (Virtanen et al. 2020), MATPLOTLIB (Hunter 2007), LIGO.SKYMAP (Singer 2018; Singer et al. 2016a,b), **show your work!** (Luger et al. 2021).

REFERENCES

- Aasi, J., et al. 2015, Classical Quantum Gravity, 32, 074001, doi: [10.1088/0264-9381/32/7/074001](https://doi.org/10.1088/0264-9381/32/7/074001)
- Abbott, B. P., et al. 2017, Class. Quant. Grav., 34, 044001, doi: [10.1088/1361-6382/aa51f4](https://doi.org/10.1088/1361-6382/aa51f4)
- Abbott, R., et al. 2021a. <https://arxiv.org/abs/2111.03634>
- . 2021b, GWTC-3: Compact Binary Coalescences Observed by LIGO and Virgo During the Second Part of the Third Observing Run — O3 search sensitivity estimates, Zenodo, doi: [10.5281/zenodo.5546676](https://doi.org/10.5281/zenodo.5546676)
- . 2021c. <https://arxiv.org/abs/2111.03606>

- 439 —. 2021d. <https://arxiv.org/abs/2108.01045>
- 440 —. 2021e, GWTC-3: Compact Binary Coalescences
441 Observed by LIGO and Virgo During the Second Part of
442 the Third Observing Run — Parameter estimation data
443 release, Zenodo, doi: [10.5281/zenodo.5546663](https://doi.org/10.5281/zenodo.5546663)
- 444 —. 2021f, GWTC-2.1 Data Release.
<https://www.gw-openscience.org/GWTC-2.1/>
- 445 —. 2021g, GWTC-3 Data Release.
<https://www.gw-openscience.org/GWTC-3/>
- 446 —. 2021h, SoftwareX, 13, 100658,
447 doi: [10.1016/j.softx.2021.100658](https://doi.org/10.1016/j.softx.2021.100658)
- 448 —. 2022, GWTC-2.1: Deep Extended Catalog of Compact
449 Binary Coalescences Observed by LIGO and Virgo
450 During the First Half of the Third Observing Run -
451 Parameter Estimation Data Release, v2, Zenodo,
452 doi: [10.5281/zenodo.6513631](https://doi.org/10.5281/zenodo.6513631)
- 453 —. 2023, The population of merging compact binaries
454 inferred using gravitational waves through GWTC-3 -
455 Data release, v2, Zenodo, doi: [10.5281/zenodo.7843926](https://doi.org/10.5281/zenodo.7843926)
- 456 Acernese, F., et al. 2015, Classical Quantum Gravity, 32,
457 024001, doi: [10.1088/0264-9381/32/2/024001](https://doi.org/10.1088/0264-9381/32/2/024001)
- 458 Anderson, W. G., Brady, P. R., Chin, D., et al. 2002, Beam
459 pattern response functions and times of arrival for
460 earthbound interferometer, Tech. Rep. LIGO-T010110,
461 LIGO Scientific Collaboration.
<https://dcc.ligo.org/LIGO-T010110/public>
- 462 Ashton, G., et al. 2019, Astrophys. J. Suppl., 241, 27,
463 doi: [10.3847/1538-4365/ab06fc](https://doi.org/10.3847/1538-4365/ab06fc)
- 464 Bohe, A., Marsat, S., Faye, G., & Blanchet, L. 2013, Class.
465 Quant. Grav., 30, 075017,
466 doi: [10.1088/0264-9381/30/7/075017](https://doi.org/10.1088/0264-9381/30/7/075017)
- 467 Cavaglia, M., & Modi, A. 2020, Universe, 6, 93,
468 doi: [10.3390/universe6070093](https://doi.org/10.3390/universe6070093)
- 469 Creighton, J., Fairhurst, S., Krishnan, B., et al. ????,
470 LALSimulation-LALInference parameter transformations.
471 https://lscsoft.docs.ligo.org/lalsuite/lalsimulation/group__lalsimulation__inference.html#ga1517b28ff879d5d1c7ba8468385e4054
- 472 Dwyer, S., Sigg, D., Ballmer, S. W., et al. 2015, Phys. Rev.,
473 D91, 082001, doi: [10.1103/PhysRevD.91.082001](https://doi.org/10.1103/PhysRevD.91.082001)
- 474 Essick, R., & Farr, W. 2022.
<https://arxiv.org/abs/2204.00461>
- 475 Essick, R., Farr, W. M., Fishbach, M., Holz, D. E., &
476 Katsavounidis, E. 2023, Phys. Rev. D, 107, 043016,
477 doi: [10.1103/PhysRevD.107.043016](https://doi.org/10.1103/PhysRevD.107.043016)
- 478 Fishbach, M., Holz, D. E., & Farr, W. M. 2018, Astrophys.
479 J. Lett., 863, L41, doi: [10.3847/2041-8213/aad800](https://doi.org/10.3847/2041-8213/aad800)
- 480 Fishbach, M., Doctor, Z., Callister, T., et al. 2021,
481 Astrophys. J., 912, 98, doi: [10.3847/1538-4357/abee11](https://doi.org/10.3847/1538-4357/abee11)
- 482 García-Quirós, C., Colleoni, M., Husa, S., et al. 2020, Phys.
483 Rev. D, 102, 064002, doi: [10.1103/PhysRevD.102.064002](https://doi.org/10.1103/PhysRevD.102.064002)
- 484 García-Quirós, C., Husa, S., Mateu-Lucena, M., &
485 Borchers, A. 2021, Class. Quant. Grav., 38, 015006,
486 doi: [10.1088/1361-6382/abc36e](https://doi.org/10.1088/1361-6382/abc36e)
- 487 Harris, C. R., et al. 2020, Nature, 585, 357,
488 doi: [10.1038/s41586-020-2649-2](https://doi.org/10.1038/s41586-020-2649-2)
- 489 Hunter, J. D. 2007, Computing In Science & Engineering,
490 9, 90, doi: [10.1109/MCSE.2007.55](https://doi.org/10.1109/MCSE.2007.55)
- 491 Isi, M. 2022. <https://arxiv.org/abs/2208.03372>
- 492 Isi, M., Farr, W. M., & Varma, V. 2023, Data and software
493 release for “The directional isotropy of LIGO-Virgo
494 binaries”. <https://github.com/maxisi/gwisotropy/>
- 495 Kidder, L. E. 1995, Phys. Rev. D, 52, 821,
496 doi: [10.1103/PhysRevD.52.821](https://doi.org/10.1103/PhysRevD.52.821)
- 497 Loredo, T. J. 2004, AIP Conf. Proc., 735, 195,
498 doi: [10.1063/1.1835214](https://doi.org/10.1063/1.1835214)
- 499 Luger, R., Bedell, M., Foreman-Mackey, D., et al. 2021,
500 arXiv e-prints, arXiv:2110.06271.
<https://arxiv.org/abs/2110.06271>
- 501 Madau, P., & Dickinson, M. 2014, Ann. Rev. Astron.
502 Astrophys., 52, 415,
503 doi: [10.1146/annurev-astro-081811-125615](https://doi.org/10.1146/annurev-astro-081811-125615)
- 504 Mandel, I., Farr, W. M., & Gair, J. R. 2019, Mon. Not.
505 Roy. Astron. Soc., 486, 1086, doi: [10.1093/mnras/stz896](https://doi.org/10.1093/mnras/stz896)
- 506 Martin, O. A., Hartikainen, A., Abril-Pla, O., et al. 2023,
507 ArviZ, v0.15.1, Zenodo, doi: [10.5281/zenodo.7703176](https://doi.org/10.5281/zenodo.7703176)
- 508 Miller, S., Callister, T. A., & Farr, W. 2020, Astrophys. J.,
509 895, 128, doi: [10.3847/1538-4357/ab80c0](https://doi.org/10.3847/1538-4357/ab80c0)
- 510 Payne, E., Banagiri, S., Lasky, P., & Thrane, E. 2020, Phys.
511 Rev. D, 102, 102004, doi: [10.1103/PhysRevD.102.102004](https://doi.org/10.1103/PhysRevD.102.102004)
- 512 Poisson, E., & Will, C. M. 2014, Gravity: Newtonian,
513 post-newtonian, relativistic (Cambridge University Press)
- 514 Pratten, G., Husa, S., Garcia-Quiros, C., et al. 2020, Phys.
515 Rev. D, 102, 064001, doi: [10.1103/PhysRevD.102.064001](https://doi.org/10.1103/PhysRevD.102.064001)
- 516 Pratten, G., et al. 2021, Phys. Rev. D, 103, 104056,
517 doi: [10.1103/PhysRevD.103.104056](https://doi.org/10.1103/PhysRevD.103.104056)
- 518 Punturo, M., et al. 2010, Class. Quant. Grav., 27, 194002,
519 doi: [10.1088/0264-9381/27/19/194002](https://doi.org/10.1088/0264-9381/27/19/194002)
- 520 Reitze, D., et al. 2019, Bull. Am. Astron. Soc., 51, 035.
<https://arxiv.org/abs/1907.04833>
- 521 Romero-Shaw, I. M., et al. 2020, Mon. Not. Roy. Astron.
522 Soc., 499, 3295, doi: [10.1093/mnras/staa2850](https://doi.org/10.1093/mnras/staa2850)
- 523 Singer, L. 2018, ligo.skymap.
<https://pypi.org/project/ligo.skymap/>
- 524 Singer, L. P., et al. 2016a, Astrophys. J. Lett., 829, L15,
525 doi: [10.3847/2041-8205/829/1/L15](https://doi.org/10.3847/2041-8205/829/1/L15)
- 526 —. 2016b, Astrophys. J. Suppl., 226, 10,
527 doi: [10.3847/0067-0049/226/1/10](https://doi.org/10.3847/0067-0049/226/1/10)

- ⁵³⁷ Stiskalek, R., Veitch, J., & Messenger, C. 2021, Mon. Not. Roy. Astron. Soc., 501, 970, doi: [10.1093/mnras/staa3613](https://doi.org/10.1093/mnras/staa3613)
- ⁵³⁸ Virtanen, P., et al. 2020, Nature Meth., 17, 261, doi: [10.1038/s41592-019-0686-2](https://doi.org/10.1038/s41592-019-0686-2)
- ⁵⁴¹ Vitale, S., Biscoveanu, S., & Talbot, C. 2022.
- ⁵⁴² <https://arxiv.org/abs/2204.00968>
- ⁵⁴³ Wiecki, T., Salvatier, J., Vieira, R., et al. 2023,
- ⁵⁴⁴ pymc-devs/pymc: v5.3.1, v5.3.1, Zenodo,
- ⁵⁴⁵ doi: [10.5281/zenodo.7868623](https://doi.org/10.5281/zenodo.7868623)

546

APPENDIX

547 A. COMPUTING THE TOTAL ANGULAR
548 MOMENTUM

549 Here we describe how to compute the total angular
 550 momentum vector \vec{J} in the celestial coordinate frame of
 551 the main text, starting from BBH parameters measured
 552 in LIGO-Virgo analyses. The total angular momentum
 553 is defined, as in Eq. (2), to be the vector sum of the
 554 orbital angular momentum \vec{L} and the dimensionful BH
 555 spins $\vec{S}_{1/2}$. We can thus compute \vec{J} by summing the
 556 components of \vec{L} and $\vec{S}_{1/2}$ in some common frame with
 557 known orientation relative to our target.

558 The Cartesian components of the BH dimensionless
 559 spins, $\vec{\chi}_{1/2} \equiv \vec{S}_{1/2}/m_{1/2}^2$ in units where $G = c = 1$, can
 560 be readily obtained from the LIGO-Virgo samples, in
 561 a frame in which the z -axis points along (the Newto-
 562 nian) \vec{L} and the x -axis points along the orbital vector
 563 from the lighter to the heavier body (Creighton et al.
 564 ????) (see, e.g., Fig. 18 in Isi 2022,); this specifica-
 565 tion is established in reference to some specific point in
 566 the evolution of the system, e.g., when the GW signal
 567 at the detector reaches some frequency f_{ref} . With that
 568 information, all we need to compute the components of
 569 \vec{J} in that same frame is the magnitude $|L|$ of the orbital
 570 angular momentum; then, the \vec{J} vector will be specified
 571 by

$$572 J_x = S_{1,x} + S_{2,x}, \quad (\text{A1a})$$

$$573 J_y = S_{1,y} + S_{2,y}, \quad (\text{A1b})$$

$$574 J_z = S_{1,z} + S_{2,z} + |L|, \quad (\text{A1c})$$

576 and $\vec{J} = J_x \hat{x} + J_y \hat{y} + J_z \hat{L}$, where $\hat{L} \equiv \vec{L}/|L|$ is the direc-
 577 tion of the orbital angular momentum, \hat{x} is the orbital
 578 vector at the reference time, and \hat{y} completes the triad.

579 In the above equations, $(S_{1/2,x}, S_{1/2,y}, S_{1/2,z})$ are the
 580 components of the dimensionful spins, which we can de-
 581 rive from the respective components of the dimension-
 582 less spins $\vec{\chi}_{1/2}$ using the masses $m_{1/2}$ and the definition
 583 above. Following the standard LIGO-Virgo calculation
 584 (Creighton et al. ????),⁶ we can approximate the magni-
 585 tude of the orbital angular momentum as (Kidder 1995;
 586 Bohe et al. 2013)

$$587 |L| = L_N (1 + \ell_{1\text{PN}}), \quad (\text{A2})$$

⁶ Here we are following the definition of $|L|$ within the LIGO-Virgo software; this is adopted in defining the inclination parameters θ_{JN} and ι . The effect of truncating the series at the first post-Newtonian order is expected to be small, but could be revisited in future work.

588 where $L_N = m_1 m_2 / v$ is the Newtonian angular mo-
 589 mentum, $v = (\pi M f_{\text{ref}})^{1/3}$ is the post-Newtonian expan-
 590 sion parameter at the reference frequency, and $\ell_{1\text{PN}} =$
 591 $v^2 (3 + \eta/3)/2$ is the first-order correction to $|L|$, for the
 592 symmetric mass ratio $\eta \equiv m_1 m_2 / M^2$ and the total mass
 593 $M \equiv m_1 + m_2$. We can then get the components of the
 594 orientation vector $\hat{J} \equiv \vec{J}/|J|$ by normalizing Eq. (A1).

595 The components of \vec{J} in Eq. (A1) are defined in a
 596 binary-specific frame which does not facilitate compar-
 597 isons across different systems. To express \vec{J} in a com-
 598 mon frame for all binaries, all we need is to express the
 599 $(\hat{x}, \hat{y}, \hat{L})$ coordinate basis of Eq. (A1) in a Celestial co-
 600 ordinate frame. We can achieve this by first obtaining
 601 the Cartesian components for \vec{L} in this frame using the
 602 measured right ascension α , declination δ , inclination ι ,
 603 polarization angle ψ , and the reference orbital phase ϕ_{ref}
 604 (see, e.g., Figs. 6 and 8 Isi 2022). In doing so, however, it
 605 is important to keep in mind that, since the polarization
 606 angle only enters the waveform as 2ψ (i.e., ψ and $\psi + \pi$
 607 are degenerate), the LIGO-Virgo analyses usually only
 608 allow $0 \leq \psi < \pi$; yet, ψ and $\psi + \pi$ are two physically dis-
 609 tinct configurations, so we must for our purposes mirror
 610 the samples to ensure they span the full range of polar-
 611 ization angles, $0 \leq \psi < 2\pi$ (or, equivalently, randomly
 612 add 0 or π to ψ for each sample).

613 Having properly accounted for this degeneracy, \hat{L} can
 614 be obtained from the source location $\hat{N} \equiv -\hat{k}$ in Eq. (1),
 615 ι and ψ via rotations and geometric products as

$$616 \hat{L} = R_{\hat{w}_y}(\iota) \hat{k}, \quad (\text{A3})$$

617 where $R_{\hat{v}}(\theta)$ is a right-handed rotation by an angle
 618 θ around some direction \hat{v} , and $\hat{w}_y \propto \hat{k} \times \hat{w}_x$ with
 619 $\hat{w}_x = R_{\hat{k}}(\psi) \hat{u}$, for \hat{u} due west (see (Anderson et al. 2002)
 620 for details). We can similarly obtain \hat{x} by rotating \hat{w}_y
 621 around \hat{L} by ϕ_{ref} , namely

$$622 \hat{x} = R_{\hat{L}}(\phi_{\text{ref}}) \hat{w}_y, \quad (\text{A4})$$

623 and $\hat{y} \propto \hat{L} \times \hat{x}$ completes the triad. This provides ex-
 624 pressions for the components of the $(\hat{x}, \hat{y}, \hat{L})$ basis for
 625 each binary in a common reference frame, from which
 626 we can obtain the components of all \hat{J} vectors in that
 627 same frame via Eq. (A1). Those components are the
 628 input for the hierarchical analysis described in the main
 629 text.

630 B. PRIOR IN UNCONSTRAINED PARAMETERS

631 Recall that we sample in parameters $\vec{u}_{N/J}$ defined by

$$632 \vec{u}_{N/J} = \frac{\vec{v}_{N/J}}{\sqrt{1 - \vec{v}_{N/J} \cdot \vec{v}_{N/J}}} \quad (\text{B5})$$

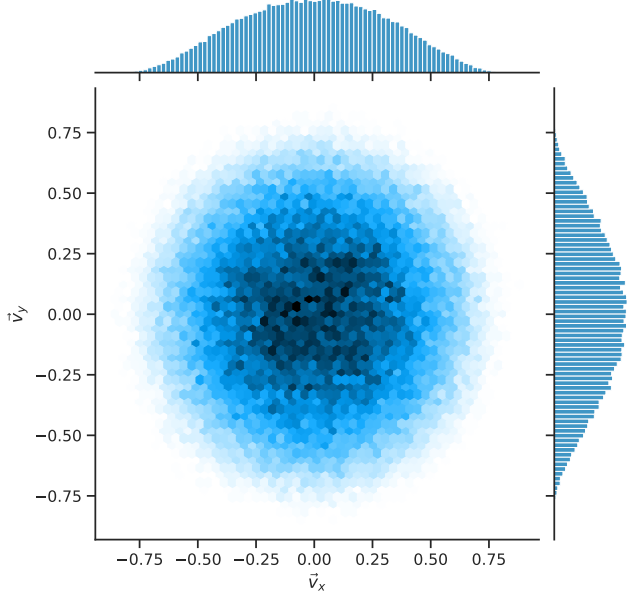


Figure 7. *Prior.* Two-dimensional slice of the Gaussian prior on the components of $\vec{v}_{J/N}$ for $\sigma = 0.4$, as used for the analysis in the main paper. With this choice, the origin is not disfavored by the three-dimensional prior probability density.

that map the unit ball \mathbb{B}^3 to \mathbb{R}^3 . A Gaussian prior with mean $\vec{0}$ and standard deviation in each component of σ on $\vec{u}_{N/J}$ induces a prior on $\vec{v}_{N/J}$ that is

$$\log p(\vec{v}_{N/J}) = \text{const} - \frac{|\vec{v}_{N/J}|^2}{2\sigma^2(1 - |\vec{v}_{N/J}|^2)} - \frac{5}{2} \log(1 - |\vec{v}_{N/J}|^2). \quad (\text{B6})$$

The derivative of the density with respect to $|\vec{v}_{N/J}|$ vanishes at the origin, as it must by symmetry. But the second derivative does not, and is

$$\frac{\partial^2 \log p}{\partial |\vec{v}_{N/J}|^2} = 5 - \frac{1}{\sigma^2}. \quad (\text{B7})$$

Thus, such a Gaussian prior will have a *maximum* at $\vec{v}_{N/J} = \vec{0}$ only if $\sigma < 1/\sqrt{5} \simeq 0.45$; otherwise it places too much prior mass on large $|\vec{u}_{N/J}|$ which generates a ring-shaped maximum in the prior for some $|\vec{v}_{N/J}| > 0$ and a *minimum* at the origin. With the desire to be uninformative about the typical scale of the components of $\vec{v}_{N/J}$ while keeping the maximum prior density at the origin, we choose $\sigma = 0.4 < 1/\sqrt{5}$ for the analysis in this paper. A two-dimensional slice of the prior on the components of $\vec{v}_{N/J}$ for this choice is illustrated in Fig. 7.

C. DIRECTION OF TOTAL ANGULAR MOMENTUM FOR INDIVIDUAL EVENTS

In Fig. 8, we present posteriors on the direction of the total angular momentum \hat{J} for all 57 events in our set. We produced these posteriors by applying the calculation described in Appendix A to the samples released by LIGO-Virgo (Abbott et al. 2022, 2021e), after reweighting as outlined in Sec. 2.2.

The skymaps in the figure provide a Molleweide projection of probability density over the celestial sphere, in the standard equatorial, geocentric coordinates used in the main text. A darker color corresponds to a direction in the sky with more probability density. From these maps, it is clear that not all events are equally informative about \hat{J} ; better constrained events will tend to dominate our hierarchical measurement.

The skymaps were produced using the LIGO.SKYMAP package (Singer 2018; Singer et al. 2016a,b), a set of standard LIGO-Virgo tools for the processing of probability densities over the sphere. We make these figures, corresponding Flexible Image Transport System (FITS) files, and code used to generate them, available in our data release (Isi et al. 2023).

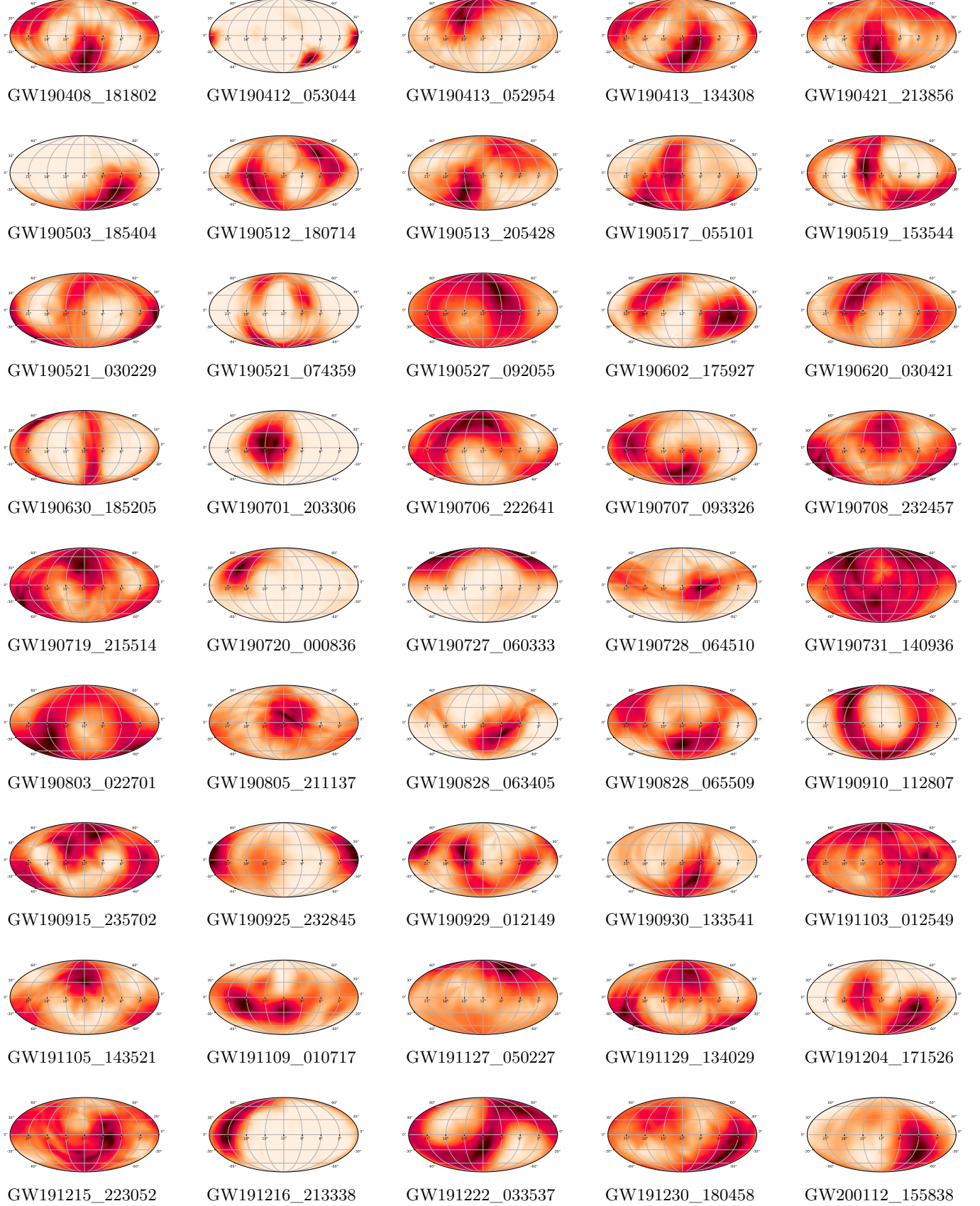


Figure 8. Measurements of the total angular momentum direction, \hat{J} , for the events in our set, in a Mollweide projection of Earth-centric Celestial coordinates; darker color represents higher probability density for that direction in space.

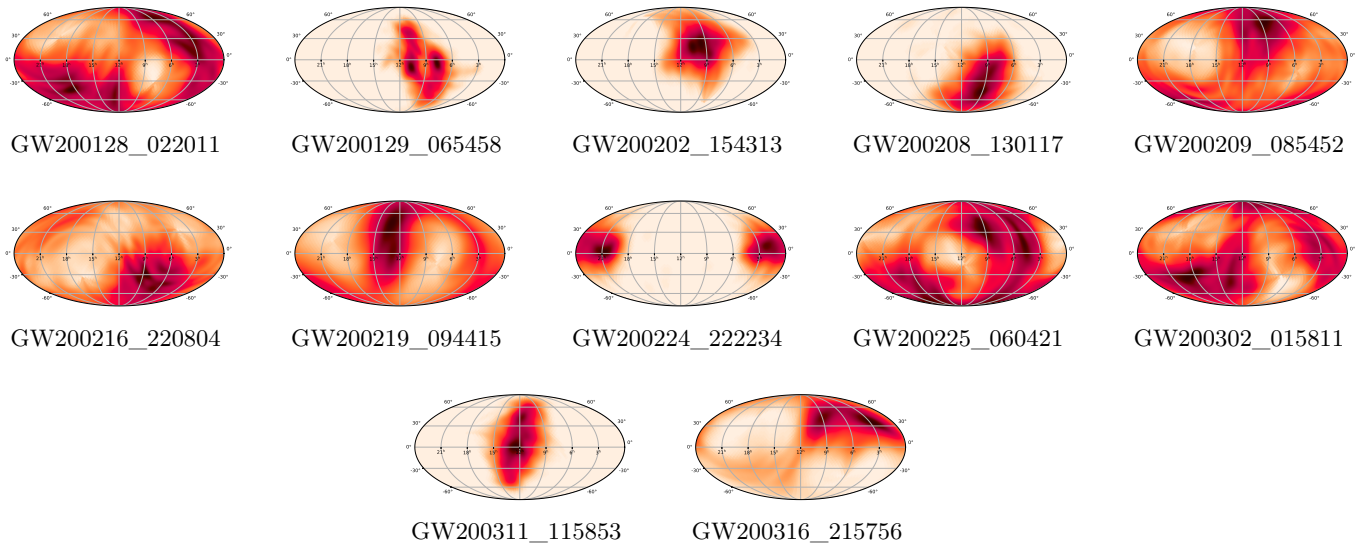


Figure 8. Measurements of the total angular momentum direction, \hat{J} , for the events in our set, in a Mollweide projection of Earth-centric Celestial coordinates; darker color represents higher probability density for that direction in space (cont.).